Resource

Cell Metabolism

SoNar, a Highly Responsive NAD$^+$/NADH Sensor, Allows High-Throughput Metabolic Screening of Anti-tumor Agents

Graphical Abstract

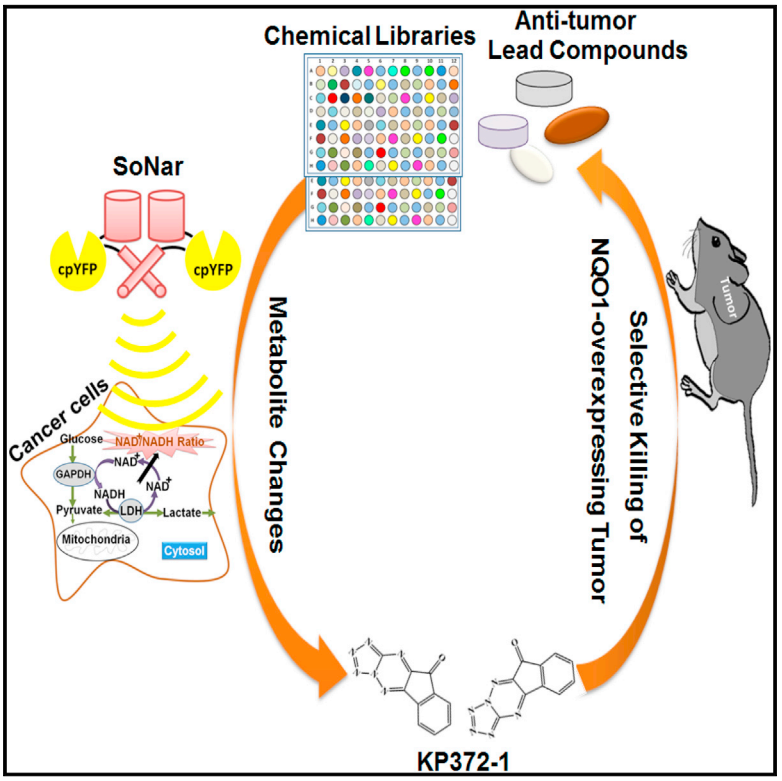

Authors

Yuzheng Zhao, Qingxun Hu, ..., Joseph Loscalzo, Yi Yang

Correspondence

yiyang@ecust.edu.cn

In Brief

Zhao et al. report the development of "SoNar," an intensely fluorescent, rapidly responsive, pH-resistant sensor for cytosolic NAD$^+$ and NADH redox states in vivo. High-throughput metabolic screening of anticancer compounds identified KP372-1 as a potent redox cycling anti-tumor agent.

Highlights

- SoNar sensor is capable of tracking subtle changes in NAD$^+$/NADH in vitro and in vivo
- SoNar enables high-throughput screening for new agents targeting tumor metabolism
- KP372-1 is identified as a potent NQO1-dependent redox cycling anti-tumor agent

Zhao et al., 2015, Cell Metabolism *21*, 777–789
May 5, 2015
http://dx.doi.org/10.1016/j.cmet.2015.04.009

Cell Metabolism
Resource

SoNar, a Highly Responsive NAD+/NADH Sensor, Allows High-Throughput Metabolic Screening of Anti-tumor Agents

Yuzheng Zhao,[1,2,3,4] Qingxun Hu,[1] Feixiong Cheng,[4] Ni Su,[1,2,4] Aoxue Wang,[1,2,4] Yejun Zou,[1,2,4] Hanyang Hu,[1] Xianjun Chen,[1,2,4] Hai-Meng Zhou,[5] Xinzhi Huang,[6] Kai Yang,[6] Qian Zhu,[1,2] Xue Wang,[1] Jing Yi,[6] Linyong Zhu,[7] Xuhong Qian,[8] Lixin Chen,[9] Yun Tang,[4] Joseph Loscalzo,[10] and Yi Yang[1,2,3,4,*]

[1]Synthetic Biology and Biotechnology Laboratory, State Key Laboratory of Bioreactor Engineering, Shanghai Collaborative Innovation Center for Biomanufacturing Technology

[2]Optogenetics & Molecular Imaging Interdisciplinary Research Center, CAS Center for Excellence in Brain Science

[3]Collaborative Innovation Center of Genetics and Development

[4]Shanghai Key Laboratory of New Drug Design, School of Pharmacy
East China University of Science and Technology, 130 Mei Long Road, Shanghai 200237, China

[5]Zhejiang Provincial Key Laboratory of Applied Enzymology, Yangtze Delta Region Institute of Tsinghua University, Jiaxing 314006, China

[6]Department of Biochemistry and Molecular Cell Biology, Key Laboratory of the Education Ministry for Cell Differentiation and Apoptosis, Institutes of Medical Sciences, Shanghai Jiao Tong University School of Medicine, 280 S. Chongqing Road, Shanghai 200025, China

[7]Key Laboratory for Advanced Materials, Institute of Fine Chemicals

[8]Shanghai Key Laboratory of Chemical Biology
East China University of Science and Technology, 130 Mei Long Road, Shanghai 200237, China

[9]Shanghai Laboratory Animal Center, Chinese Academy of Sciences, Shanghai 201615, China

[10]Department of Medicine, Brigham and Women's Hospital, Harvard Medical School, Boston, MA 02115, USA

*Correspondence: yiyang@ecust.edu.cn

http://dx.doi.org/10.1016/j.cmet.2015.04.009

SUMMARY

The altered metabolism of tumor cells confers a selective advantage for survival and proliferation, and studies have shown that targeting such metabolic shifts may be a useful therapeutic strategy. We developed an intensely fluorescent, rapidly responsive, pH-resistant, genetically encoded sensor of wide dynamic range, denoted SoNar, for tracking cytosolic NAD+ and NADH redox states in living cells and in vivo. SoNar responds to subtle perturbations of various pathways of energy metabolism in real time, and allowed high-throughput screening for new agents targeting tumor metabolism. Among > 5,500 unique compounds, we identified KP372-1 as a potent NQO1-mediated redox cycling agent that produced extreme oxidative stress, selectively induced cancer cell apoptosis, and effectively decreased tumor growth in vivo. This study demonstrates that genetically encoded sensor-based metabolic screening could serve as a valuable approach for drug discovery.

INTRODUCTION

In recent years, there is renewed attention paid to Otto Warburg's observation in 1924 that cancer cells shift energy metabolism from mitochondrial oxidative phosphorylation to aerobic glycolysis (Warburg, 1956). Cancer cell metabolism is dramatically reprogrammed to support energy demand and increased biosynthesis of macromolecules for rapid cell proliferation, which has attracted many efforts to target it as a selective anticancer strategy (Cairns et al., 2011; Vander Heiden, 2011; Vander Heiden et al., 2009). Biochemical methods, including enzymatic cycling assays, chromatography, mass spectrometry, and nuclear magnetic resonance spectroscopy, can be used to assess cellular metabolism and search for new cancer-targeting agents. Most of these methods require cell lysis, are time intensive, and, therefore, are not suitable for quantitative, real-time high-throughput screening. High-throughput screening of such agents in cells or in vivo is much more difficult and rarely reported. The use of genetically encoded fluorescent sensors may be a more suitable approach for metabolic chemical screening. To date, these sensors have been developed for single-cell real-time monitoring of several key metabolites (Zhao and Yang, 2015). Among these metabolites, NAD^+ and its reduced form, NADH, are the most important cofactors involved in energy metabolism. Recently, Yellen's group and our group independently developed genetically encoded NADH sensors that allow specific monitoring of dynamic changes in NADH levels in cytosol or mitochondria as affected by different metabolic states (Hung et al., 2011; Zhao et al., 2011). These Frex sensors (Zhao et al., 2011) specifically report NADH levels over a large dynamic range; however, they do not adapt an optimal tertiary structure in some cells, and their fluorescence is pH sensitive. Peredox sensors (Hung et al., 2011) are much more pH resistant and partially reflect the more physiologically relevant NAD^+/NADH ratio; however, they have a limited dynamic range, and their affinity appears too high to be useful under physiological conditions. Importantly, neither Frex nor Peredox sensors show obvious fluorescence response to NAD^+. Such limitations make it difficult

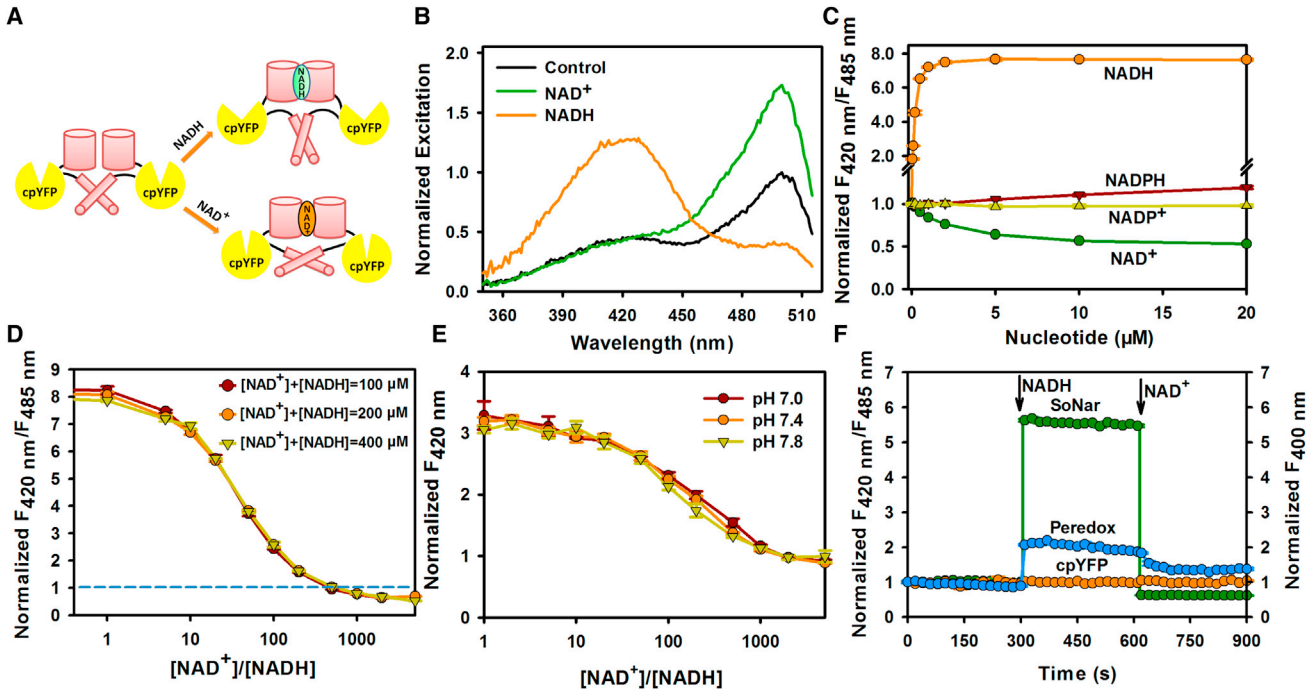

Figure 1. Genetically Encoded Sensor for NAD$^+$, NADH, and Their Ratio

(A) Design of SoNar, which is a fusion of cpYFP and the NADH-binding domain of T-Rex. Binding of NAD$^+$ or NADH induces changes in protein conformation and fluorescence.

(B) Excitation spectra of purified SoNar in the control condition (black), and after addition of 20 μM NAD$^+$ (green) or 20 μM NADH (orange), normalized to the peak intensity in the control condition. Emission was measured at 530 nm.

(C) Normalized ratio of fluorescence intensities excited at 420 nm and 485 nm (F420 nm/F485 nm) in the presence of different concentrations of NADH and its analogs.

(D) Fluorescence ratios plotted against the NAD$^+$/NADH ratio at the indicated total nicotinamide adenine dinucleotide concentration. Fluorescence ratios were normalized to the control condition in the absence of nucleotides.

(E) Fluorescence excited at 420 nm plotted against the NAD$^+$/NADH ratio at the indicated pH. Fluorescence was normalized to the control condition in the absence of pyridine nucleotides at pH 7.4.

(F) Kinetics of fluorescence response of purified SoNar, Peredox, and cpYFP protein to sequential addition of 0.2 μM NADH and 2 mM NAD$^+$. In (C)–(F) error bars represent SEM. See also Figure S1 and Table S1.

to use these sensors for measuring metabolic states in vivo and in high-throughput screening.

Herein, we report the development of an intensely fluorescent, rapidly responsive, pH-resistant, genetically encoded sensor of wide dynamic range, denoted SoNar, for the detection of cytosolic NAD$^+$ and NADH redox states in living cells and in vivo. This sensor of superior properties allowed high-throughput metabolic screening of > 5,500 unique compounds in cancer cell lines. We found that many compounds that increased the NAD$^+$/NADH ratio exhibited marked cancer cell cytotoxicity. Among them, KP372-1, the most potent in increasing NAD$^+$/NADH ratio and cancer cell killing, also effectively decreases tumor growth in vivo. Further studies revealed that KP372-1 is an NQO1-catalyzed, NAD(P)H-consuming redox cycling agent that produces extreme oxidative stress in cancer cells.

RESULTS

Generation of a Genetically Encoded Fluorescent Sensor for Detection of NAD$^+$, NADH, and Their Ratio

A total of 15 chimeric proteins were designed, in which cpYFP was inserted between two complete or truncated subunits of Rex protein from *Thermus aquaticus* (T-Rex), or between amino acid residues located on surface loops of T-Rex (Figure S1A). Among them, the chimera with cpYFP inserted after Phe189 of T-Rex showed a 300% increase in the ratio of fluorescence when excited at 420 nm and 485 nm upon NADH addition (Figure S1B). We then created a series of truncated variants of this protein, either with or without the DNA-binding domain of T-Rex, targeting residues involved in the linker between Rex and cpYFP (Figures S1C and S1D), and found the D2-C2N0 variant to manifest the most dramatic increase in the fluorescence ratio when excited at 420 and 485 nm in the presence of NADH (Figures 1A, 1B, and S1D–S1G). Intriguingly, in the presence of saturating NAD$^+$, D2-C2N0 exhibited marked increase in fluorescence when excited at 485 nm (Figures 1B and S1G).

Fluorescence titration studies showed that D2-C2N0 had an apparent dissociation constant (K_d) ~5.0 μM and ~0.2 μM, respectively, for NAD$^+$ and NADH at pH 7.4 (Figure 1C), far below the total intracellular pool of NAD$^+$ and NADH in the range of hundreds micromolar (Yamada et al., 2006; Yang et al., 2007). Intracellularly, the sensor would be occupied by either NAD$^+$ or NADH molecules, and its steady-state fluorescence would report the NAD$^+$/NADH ratio rather than

the absolute concentrations of the two nucleotides (Figure 1D). We find that D2-C2N0 has an apparent $K_{NAD^+/NADH}$ of ~40, the ratio of NAD^+ and NADH at which the response is half-maximal, and is analogous to the K_d of a "receptor" for the redox couple. The sensor has high selectivity toward the NAD^+/NADH ratio, showing no apparent fluorescence changes toward or in the presence of analogs like $NADP^+$, NADPH, ATP, or ADP (Figures 1C and S1H–S1J). The opposing directional changes of D2-C2N0 fluorescence in the presence of NAD^+ and NADH rendered a 15-fold dynamic range, making the sensor among the most responsive genetically encoded sensors available to date (Figure 1D). D2-C2N0 fluorescence excited at 420 nm was much less sensitive to pH, allowing the measurement of NADH levels when modest pH fluctuations occur (Figure 1E). By contrast, D2-C2N0 fluorescence when excited at 485 nm was sensitive to pH, but its dynamic range and K_R are more pH resistant (Figures S1K and S1L). Thus, the pH effects can be alternatively corrected by measuring D2-C2N0's and cpYFP's fluorescence in parallel, owing to their very similar pH responses (Figures S1L and S1M). Furthermore, kinetic studies showed that the fluorescence of D2-C2N0 responded immediately to sequential addition of NADH and NAD^+ (Figure 1F), suggesting its usefulness in real-time measurements. Collectively, these data show that D2-C2N0 is highly sensitive and selective for NAD^+ and NADH, has rapid responses and a large dynamic range, and is an effective ratiometric sensor for NAD^+, NADH, and their ratio with its uniquely designed structure. We therefore termed it SoNar (sensor of NAD(H) redox), and used it for all subsequent experiments.

Select Tumor Cell Lines Exhibit Decreased NAD^+/NADH Redox State

In H1299 human lung cancer cells, SoNar demonstrated much more intense fluorescence compared to the Frex sensor and to a palette of other genetically encoded sensors (Figure S2A), owing to its robust folding and short coding sequence. In cytosol, pyruvate and lactate are generally believed to be in equilibrium with free NAD^+ and NADH through the catalytic action of lactate dehydrogenase (LDH). In cells stably expressing SoNar, exogenous pyruvate induced an instantaneous, up to 3-fold decrease in the ratio of fluorescence with excitation at 420 and 485 nm, which then recovered slowly (Figures 2A, 2B, and S2B). Such effects of pyruvate were almost completely inhibited by the monocarboxylate transporter inhibitor AR-C155858 or LDH inhibitor oxamate (Figure 2D). In control experiments, fluorescence changes were significantly smaller for Frex and Peredox sensors, and occurred much more slowly for the Peredox sensor (Figures S2B and S2C). The more rapid responses of SoNar were due to the faster dissociation rate of the SoNar-NADH complex (Figure 1F). The LDH inhibitor oxamate increased the ratio of SoNar's fluorescence more effectively than lactate (Figures 2C, S2D, and S2E). When cells were treated with pyruvate and oxamate simultaneously, the ratio of SoNar's fluorescence rapidly decreased initially, and then gradually increased similarly to that caused by oxamate alone (Figure 2C). These data suggest that pyruvate immediately increases the cellular NAD^+/NADH ratio, while inhibition of LDH blocked NAD^+ recycling and gradually decreased the cellular NAD^+/NADH ratio, consistent with previous reports (Le et al., 2010).

We then quantified the cytosolic NAD^+/NADH ratio utilizing SoNar's fluorescence (Figures 2E, S2F, and S2G). The results showed heterogeneity among both cancer cells and non-cancer cells. H1299 and several other cancer cell lines showed significantly lower NAD^+/NADH ratios. In these cells, the LDH inhibitor was more potent than mitochondrial NADH oxidase inhibition in reducing the NAD^+/NADH ratio, whereas in non-cancer cells, a malate-aspartate shuttle inhibitor was less potent than the mitochondrial NADH oxidase inhibitor in decreasing the NAD^+/NADH ratio (Figure 2F). These results suggest that H1299 cells are highly dependent on glycolysis; mitochondrial respiration is sufficiently functional to oxidize NADH derived from glycolysis, but not NADH derived from the TCA cycle. Further studies showed that inhibition of glycolysis with 3-bromopyruvate (3-BrPA) markedly increased, whereas glucose supplementation decreased, the intracellular NAD^+/NADH ratio (Figures S2H–S2J). The glucose concentration for the half-maximal SoNar fluorescence response is ~0.26 mM in H1299 cells and ~1.4 mM in HEK293 cells (Figure S2J), again suggesting that these cancer cells had higher glycolytic activity utilizing lower concentrations of glucose and thereby maintaining their cytosolic NAD^+/NADH ratio.

The intense fluorescence of the SoNar sensor allows imaging of cellular redox states in vivo. To this end, nude mice were subcutaneously (s.c.) inoculated with H1299 cells stably expressing SoNar or cpYFP, and imaged when the tumor reached 0.6–1.2 cm. When the mice received an intravenous injection of 110 mg/kg sodium pyruvate, with excitation at 420 and 490 nm, the ratio of SoNar fluorescence in the tumor decreased immediately and then gradually recovered over 25 min (Figures 2G and 2I), suggesting that pyruvate in the blood stream significantly affected the NAD(H) redox state in the tumor tissue. In contrast, tumor tissue expressing cpYFP instead of SoNar showed no obvious fluorescence changes upon pyruvate injection, thereby excluding the possibility of interference of the sensor's fluorescence due to pH variations (Figures 2H and 2I). Taken together, these data indicate that the SoNar sensor displays a superior response, fluorescence intensity, and large dynamic range, and is very useful for the real-time tracking of subtle differences in cellular metabolic and redox states in vitro and in vivo.

SoNar-Based High-Throughput Screening for Compounds Affecting Cancer Cell Metabolism

To identify drugs that selectively target cancer cell metabolism, we screened 23 libraries of > 5,500 unique compounds from commercial libraries according to their effects on the intracellular NAD^+/NADH redox state of H1299 cells reported by the SoNar sensor (Figures 3A, 3B, and S3A; Table S2). An index was established to describe the intracellular metabolic variation induced by different compounds. While the majority of these compounds have close to zero index and, therefore, minimal impact on SoNar fluorescence and the cellular NAD^+/NADH redox state, we did identify 78 compounds that significantly decreased the NAD^+/NADH ratio in H1299 cells (index > 0.2, ~1.4% of total library) and 12 compounds that significantly increased the NAD^+/NADH ratio in H1299 cells (Figures 3B, 3C, and S3B; Table S2). The majority of the compounds that increased (8 of 12) the NAD^+/NADH ratio exhibited obvious H1299 cell toxicity (Figures 3C–3E, S3D, and S3E), while only a small fraction of the compounds that decreased (9 of 78) the NAD^+/NADH ratio

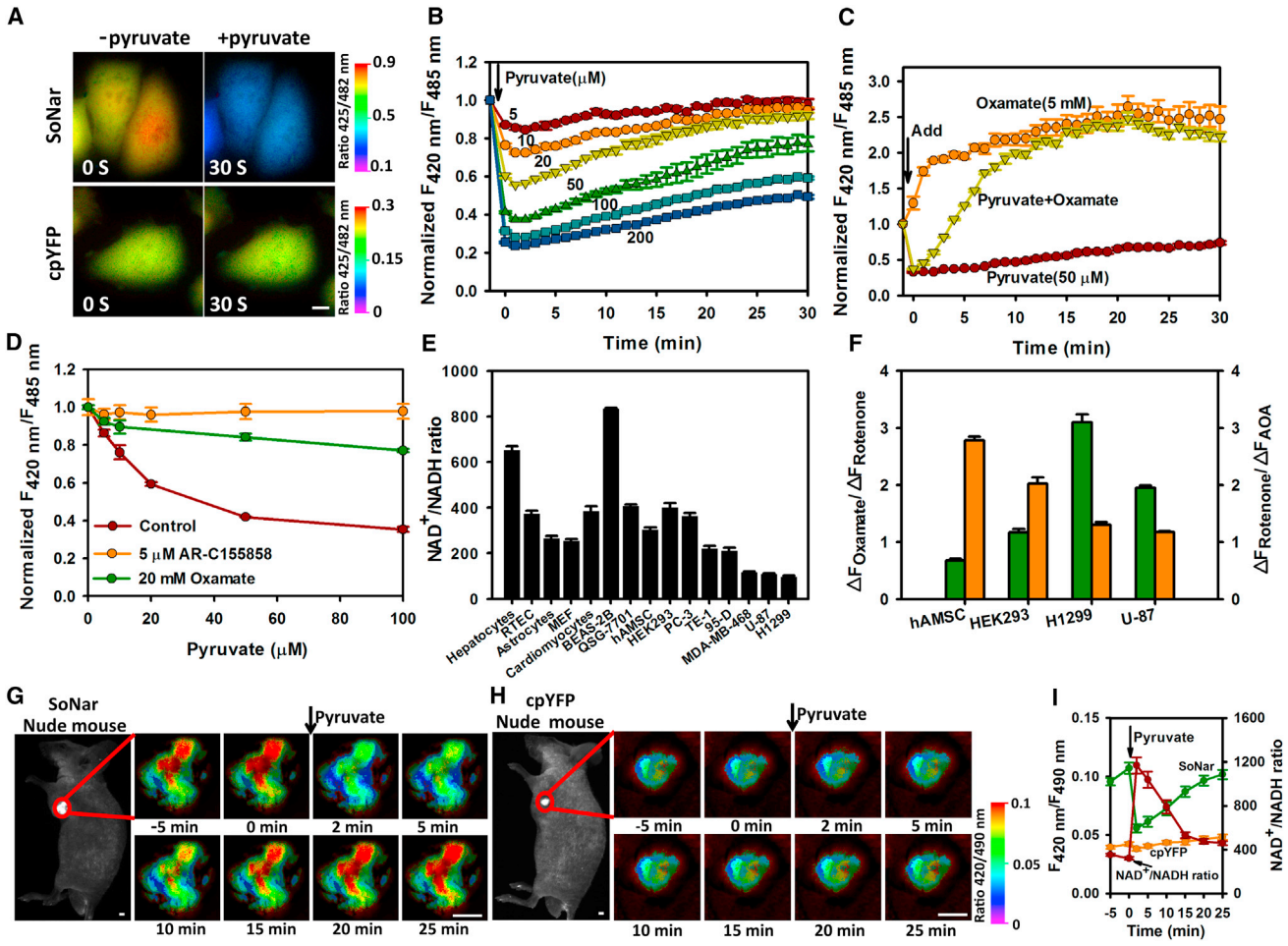

Figure 2. Imaging and Quantifying the NAD$^+$/NADH Ratio in Living Cells and In Vivo

(A) Fluorescence images of SoNar or cpYFP-expressing cells before and immediately after incubation with 1 mM pyruvate. Images were pseudocolored with the ratio of fluorescence excited at 425 nm and 482 nm. Scale bar, 10 μm.

(B) Kinetics of SoNar fluorescence responses in H1299 cells treated with exogenous pyruvate.

(C) Kinetics of SoNar fluorescence responses in H1299 cells treated with pyruvate, oxamate, or pyruvate and oxamate. Data were obtained with a fluorescence plate reader.

(D) SoNar fluorescence responses in H1299 cells treated with pyruvate were blocked by AR-C155858 or oxamate. Data were normalized to samples without pyruvate addition.

(E) NAD$^+$/NADH ratio in different primary cell cultures and cell lines quantified according to SoNar fluorescence.

(F) Effect of oxamate, rotenone, and AOA on fluorescence ratios of different cells expressing SoNar. Cells were treated with inhibitors for 10 min. Green, $\Delta F_{Oxamate}/\Delta F_{Rotenone}$; orange, $\Delta F_{Rotenone}/\Delta F_{AOA}$.

(G and H) In vivo fluorescence imaging of H1299 xenografts expressing SoNar or cpYFP in response to intravenously administered pyruvate. Sequential frames of fluorescence images of SoNar (G) or cpYFP (H) pseudocolored to the fluorescence ratio. Scale bar, 2 mm.

(I) Quantification of the NAD$^+$/NADH ratio in H1299 xenografts according to the SoNar fluorescence data in (G) and (H); error bars represent SD. All experiments performed in H1299 cells, and error bars represent SEM unless otherwise indicated. See also Figure S2.

exhibited obvious cell toxicity (Figures S3B and S3C). It is interesting that three of eight of these compounds—β-lapachone, shikonin, and fascaplysin—were potent, widely studied antitumor agents. β-lapachone was known to affect cell metabolism by redox cycling and consuming NAD(P)H (Pink et al., 2000), while shikonin was reported to inhibit pyruvate kinase M2 (Chen et al., 2011); however, as far as we are aware, the other compounds have never been directly linked to energy metabolism. Of particular note is the Akt inhibitor, also known as KP372-1 (Figure 3F). This compound is not only the most potent agent in increasing the NAD$^+$/NADH ratio, but also the most potent cancer cell cytotoxic compound, which decreased the viability of a wide range of cancer cells of different origin at concentrations as low as 100 nM. Importantly, and by contrast, the compound showed low toxicity toward various primary cells (Figures 3B, 3C, and 3G).

KP372-1 Affects Tumor Metabolism and Suppresses Tumor Growth In Vivo

We then proceeded to study the effect of KP372-1 on tumor metabolism in vivo. Pharmacokinetic studies after a single intravenous or intragastric dose (Figure S4A) demonstrated that

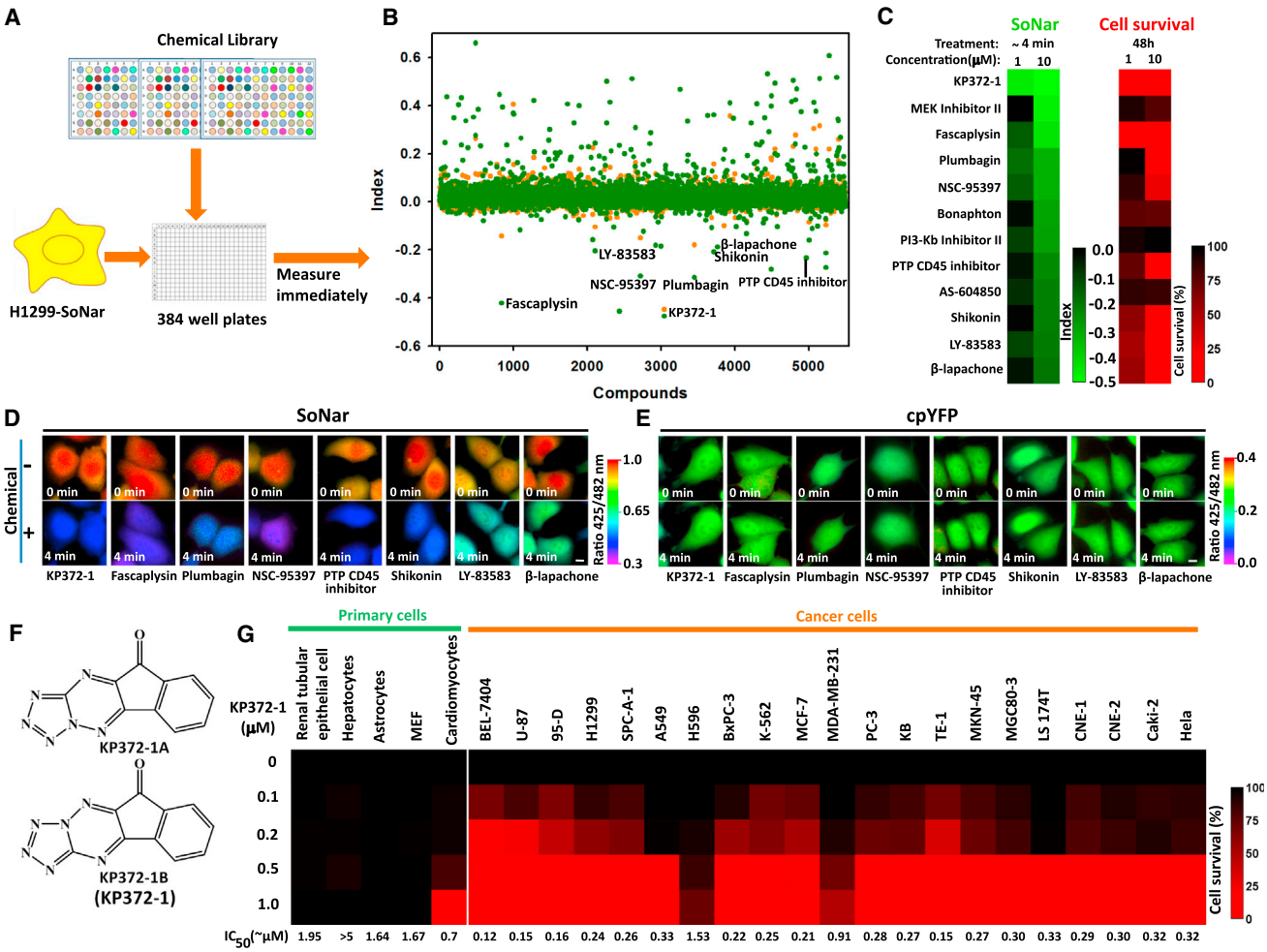

Figure 3. SoNar-Based High-Throughput Screen for Compounds Affecting Cancer Cell Metabolism

(A) Schematic of the drug screen. H1299 cells expressing SoNar were incubated with compounds in 384-well plates for 4 min and fluorescence measured.

(B) Effects of 5,501 compounds on the index ratio, $(Z_{Compound}-Z_{Control})/(Z_{Oxamate}-Z_{Pyruvate})$. The mean value and SD of the experimental population screened is expressed as Z_{Scores}. Orange, low concentration; green, high concentration.

(C) The 12 lowest indexed hits that increase intracellular NAD^+/NADH ratio and their effects on cell viability.

(D and E) Fluorescence images of H1299 cells expressing SoNar (D) or cpYFP (E) before and 4 min after treatment with different hit compounds (10 μM). Images were pseudocolored with the ratio of fluorescence excited at 425 nm and 482 nm. Scale bar, 10 μm.

(F) Chemical structure of KP372-1.

(G) Effects of different concentrations of KP372-1 on the viability of 5 primary cell cultures and 21 cancer cells. All experiments were performed in H1299 cells unless otherwise indicated. See also Figure S3 and Table S2.

KP372-1 has good bioavailability with relatively low clearance, a long half-life, and good volume of distribution (Table S3). In tumor-bearing mice in which H1299 cells stably expressing SoNar were s.c. implanted, administration of KP372-1 by tail vein injection significantly decreased the ratio of SoNar fluorescence with excitation at 420 and 490 nm in the tumor (Figures 4A and S4B), an effect that did not recover during the 1-hr time course of observation. As a control, minimal changes of fluorescence were observed in cpYFP-expressing tumor tissues with KP372-1 treatment (Figures 4B and S4B). These results suggest that KP372-1 readily enters tumor tissue and induces persistent oxidation of NADH in cancer cells (Figure 4C).

We next observed that KP372-1 profoundly suppressed the growth of the H1299 xenografts implanted s.c. into nude mice versus vehicle (Figures 4D, 4E, and S4C). Staining sections of harvested xenografts revealed that KP372-1 reduced proliferation (Ki67 staining), increased caspase-3 activity, and induced apoptosis (TUNEL staining) (Figure S4D), consistent with in vitro studies showing that KP372-1 increases apoptosis and caspase-3 activation in H1299 cells (Figures S4E–S4G). KP372-1-treated H1299 cells showed significant mitochondrial membrane permeabilization and enhanced Bax localization in mitochondria, suggesting apoptosis occurred through a mitochondrial pathway (Figures S4H and S4I). These characteristics of mitochondrial apoptosis also occurred in KP372-1-treated A549 cells, another non-small-cell lung cancer (NSCLC) cell line (Figures S4J–S4M).

No toxic effects or other indicators of illness, including significant weight loss (Figure S4N) or tissue damage (macroscopic or

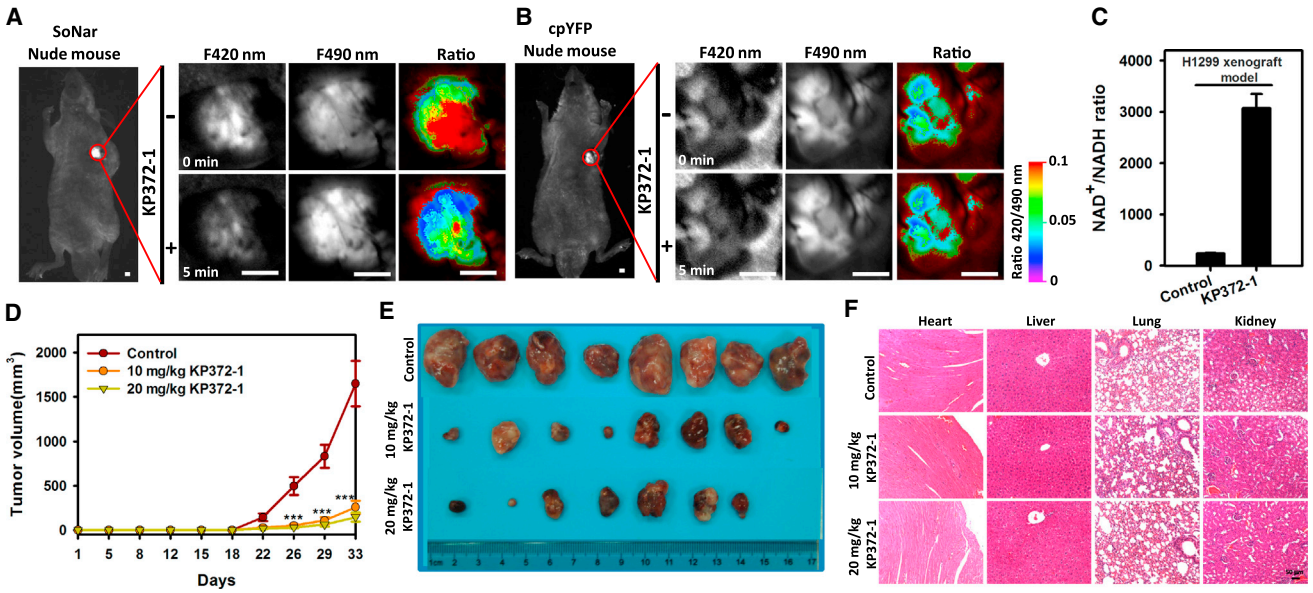

Figure 4. KP372-1 Induces NADH Oxidation and Impairs Tumor Growth In Vivo without Apparent Toxicity

(A and B) In vivo ratiometric fluorescence imaging of H1299 xenografts expressing SoNar (A) or cpYFP (B) in response to KP372-1. Images were pseudocolored with the ratio of fluorescence excited at 420 nm and 490 nm. Scale bar, 2 mm.

(C) Quantification of the NAD^+/NADH ratio in H1299 xenografts according to SoNar fluorescence. Error bars represent SD.

(D) H1299 tumor-growth curves of untreated or KP372-1-treated mice. Error bars denote SEM (n = 8 in each group).

(E) Photographs of tumors after dissection at day 33.

(F) H&E staining for the indicated tissues in animals treated with vehicle, 10 mg/kg KP372-1, or 20 mg/kg KP372-1 daily for 33 days. See also Figure S4 and Table S3.

microscopic), were observed in these mice. Pathological review of sections and an apoptosis assay of heart, liver, lung, and kidney also showed no signs of cytotoxicity (Figures 4F and S4P). The results of blood, liver, and kidney function tests were also normal (Figure S4O). These studies suggest the safety of KP372-1 for use as anticancer therapy.

KP372-1 Induces Significant Oxidative Stress and Activates the Pentose Phosphate Pathway

We performed metabolomic analysis to gain insight into how KP372-1 affected cancer cell metabolism, and identified 269 metabolites of known identity (Figures 5A and S5A; Table S4). Most prominently, many intermediates in the pentose phosphate pathway (PPP) increased 7- to 8-fold at 5 min and sustained these elevations at 60 min in response to KP372-1 (Figure 5A; Table S4). There were minimal changes in the levels of glycolytic metabolites, including lactate, in response to KP372-1, with the exception of a precipitous decrease of fructose-1,6-diphosphate (Figure 5A; Table S4). Biochemical analysis of cell culture medium and cell lysate indicated that both intracellular and extracellular lactate production remained constant (Figures S5C and S5F), again suggesting that direct perturbation of glycolysis was not significant. Biochemical analysis showed that both intracellular and extracellular pyruvate increased significantly in response to KP372-1 treatment (Figures S5B and S5E), consistent with the increased cytosolic NAD^+/NADH ratio (Figure S5D). For metabolites involved in the TCA cycle, α-ketoglutarate and succinate increased at 5 min and further increased by 60 min (Figure 5A), suggesting cumulative effects over time. Metabolomic studies validated the decrease of NADH level and increase of NAD^+ level. KP372-1 also markedly lowered glutathione (GSH) levels and elevated $NADP^+$ and oxidized GSH (GSSG) levels (Figures 5B and S5G). Although NADPH was not identified in the metabolomic analysis, conventional biochemical assay showed that cellular NADPH levels decreased 4.5-fold, whereas $NADP^+$ levels increased 4.5-fold after 5 min of KP372-1 treatment (Figures 5C and 5D).

The dose-dependent effects of KP372-1 on intracellular NADH, H_2O_2, and disulfide redox state were further explored by genetically encoded sensors, including SoNar, Hyper (Belousov et al., 2006), and roGFP1 (Dooley et al., 2004). KP372-1 induced significant oxidative stress via oxidizing NADH, generating H_2O_2, and oxidizing thiols to disulfides, respectively, two to three orders of magnitude more efficiently than H_2O_2 or thiol oxidants, such as aldrithiol-2 and diamide (Figures 5E–5G, S5H–S5J, S5L, and S5M). In controls, none of these compounds affected the fluorescence of cpYFP-expressing cells (Figure S5K). Kinetic studies showed that the decrease of NADH occurred immediately after KP372-1 addition, followed by H_2O_2 production and then thiol oxidation (Figure S5N). Overall, these results suggest that KP372-1 has a prominent impact on cellular redox state with NAD(P)H oxidation being the vanguard event. Oxidative stress is necessary for KP372-1-induced cell death, which was largely blocked by overexpressing catalase in the cell, or by treating the cell with N-acetylcysteine, a general antioxidant, or Tiron, a cell-permeable superoxide scavenger (Figures S5O and S5P).

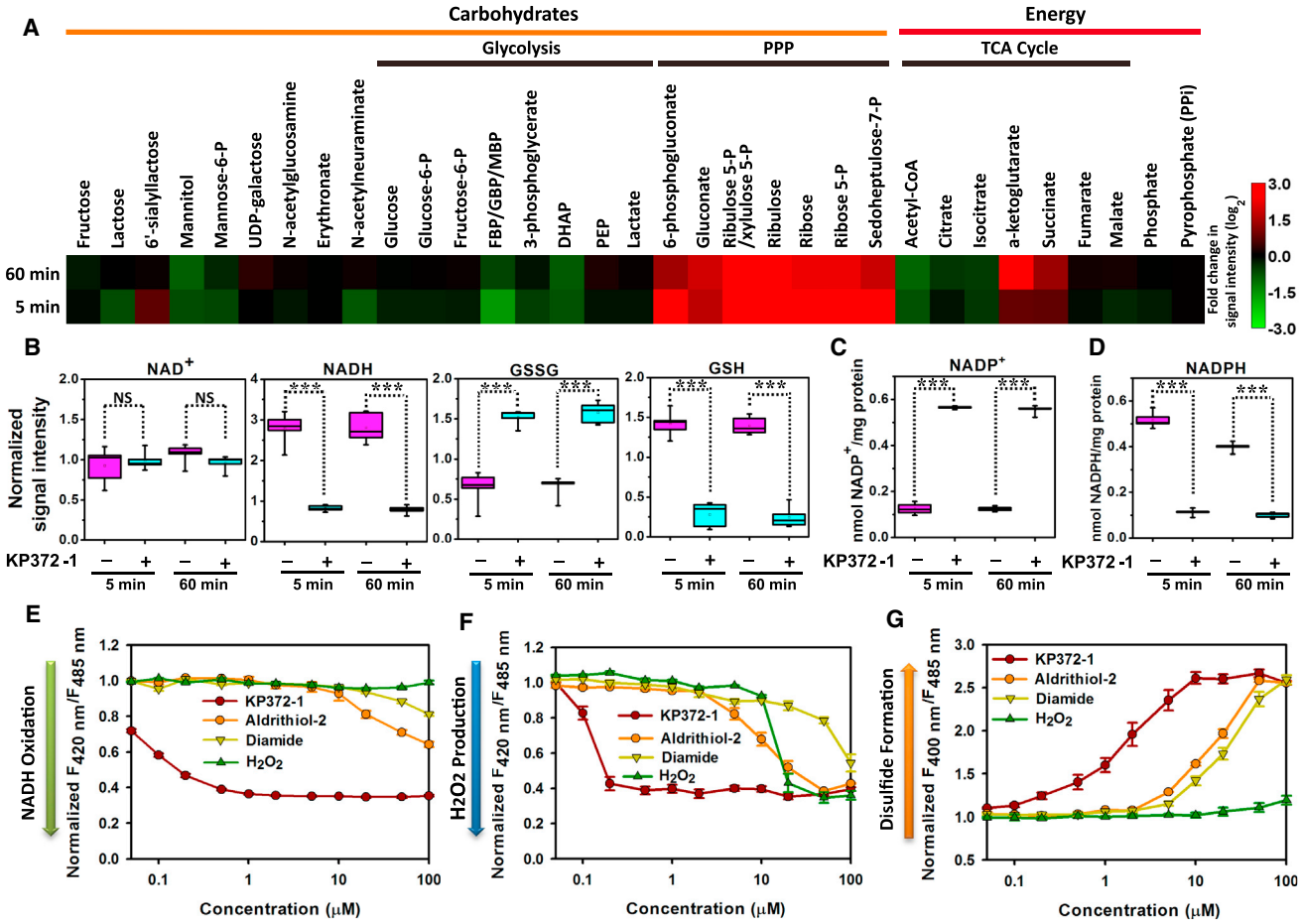

Figure 5. KP372-1 Induces Significant Oxidative Stress and Activates the Pentose Phosphate Pathway

(A) Metabolite profiles of KP372-1-treated cells shown as a heatmap. Increased metabolite concentrations are shown in red, whereas decreased metabolite concentrations are shown in green. H1299 cells were treated with 5 μM KP372-1 for 5 min and 60 min, respectively.

(B) KP372-1-induced oxidation of intracellular NADH and GSH. Data obtained by metabolomic studies as in (A) (n = 5 in each group). ***$p < 0.001$. NS, not significant.

(C and D) Intracellular $NADP^+$ (C) and NADPH (D) levels with or without 5 μM KP372-1 in H1299 cells. Data obtained by a single extraction method and in vitro biochemical assay (n = 5 in each group). ***$p < 0.001$. NS, not significant.

(E–G) Fluorescence responses of cells expressing SoNar (E), Hyper (F), and roGFP1 (G) to different concentrations of KP372-1 and other oxidants. Fluorescence was measured immediately after chemical addition and normalized to the control condition. All experiments were performed in H1299 cells; error bars represent SEM. See also Figure S5 and Table S4.

NQO1 Catalyzes NAD(P)H-Dependent KP372-1 Redox Cycling and Promotes Cancer Cell Death

We considered that KP372-1 may activate NAD(P)H-dependent reactive oxygen species (ROS)-generating enzymes in view of its potency in inducing oxidative stress, and explored the functions of such oxidases by overexpressing them in H1299 cells (Figures 6A, S6A, and S6F). We found that only overexpression of NQO1 boosted KP372-1's effects on intracellular NADH oxidation, H_2O_2 production, thiol oxidation, and cell death (Figures 6A, S6A, and S6C). NQO1 is a promising therapeutic target in cancer therapy and highly expressed in many cancer cell lines (Bey et al., 2007; Cullen et al., 2003; Pink et al., 2000), including the A549 NSCLC cell line (Bey et al., 2007) (Figure S6H). In A549 cells, KP372-1-induced oxidative stress and cell death were largely inhibited by dicoumarol, a known inhibitor of NQO1 (Pink et al., 2000) (Figures 6B, S6B, and S6D). In contrast, pharmacologic inhibitors of NAD(P)H oxidase, ENOX1, ENOX2, NQO2, mitochondrial respiratory chain complex I, xanthine oxidase, and nitric oxide synthase showed minimal effects on KP372-1-induced oxidative stress and cell death (Figures 6B and S6B). Consistent with the SoNar measurement, data calculated from the measured concentrations of the pyruvate and lactate, and the equilibrium constants of LDH (Williamson et al., 1967), also showed that cytosolic NAD^+/NADH ratio was dose-dependently increased in the cells treated with KP372-1, which is promoted by NQO1 expression (Figure S6E) or repressed by the NQO1 inhibitor dicoumarol (Figure S6G). We next generated isogenic, NQO1 knockout A549 cell lines using the CRISPR-Cas9 system (Cong et al., 2013; Ran et al., 2013). These NQO1 knockout lines, confirmed by sequencing and western blotting, were much more resistant to oxidative stress and cell death induced by KP372-1 (Figures 6C–6G and S6I).

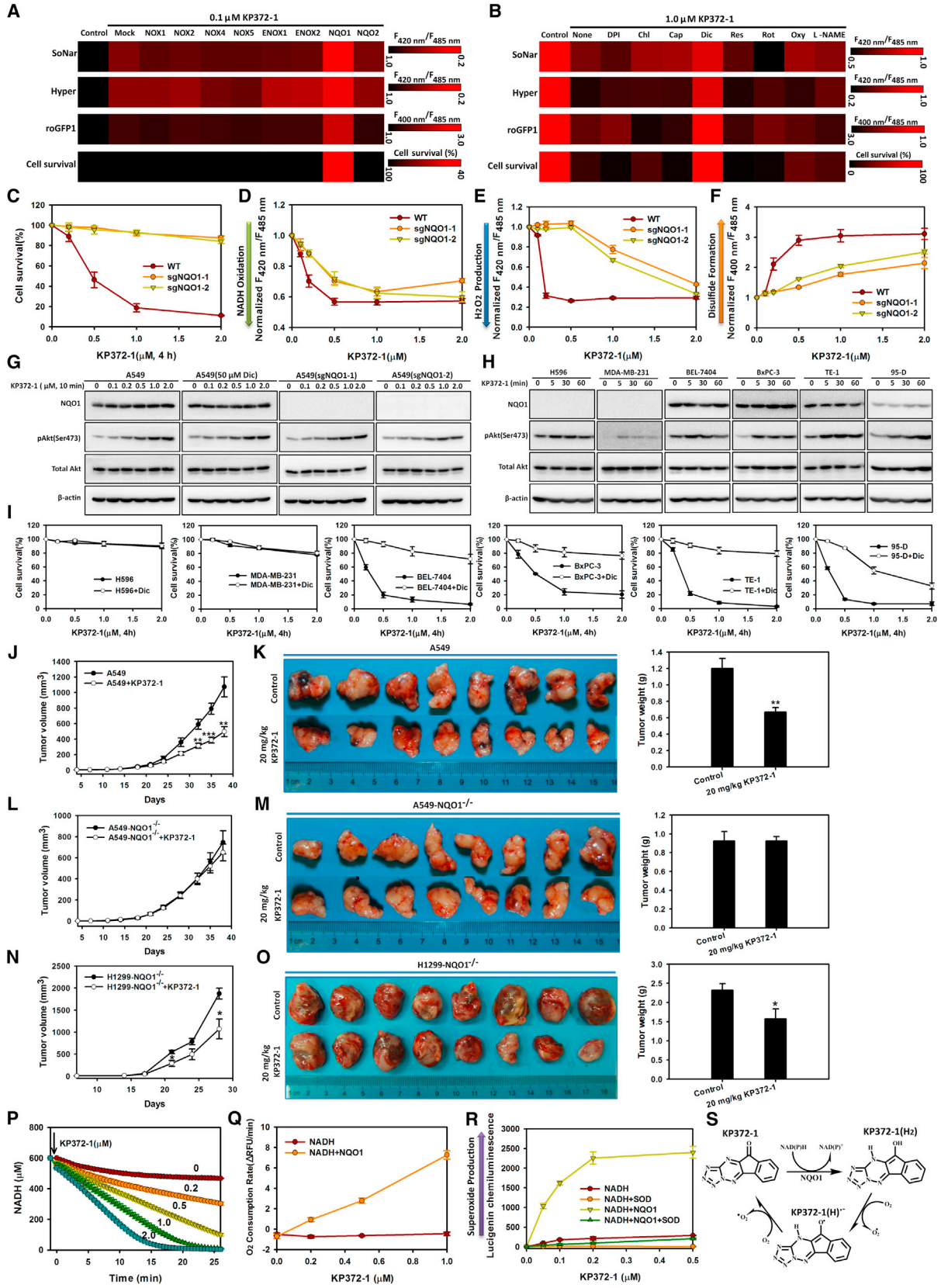

(legend on next page)

Similarly, these NQO1 knockout lines were also much more resistant to oxidative stress and cell death induced by β-lapachone (Figure S6J), another hit compound in our screen (Figures 3B and 3C) and an anti-tumor agent known to target to NQO1 (Bey et al., 2007; Pink et al., 2000). Interestingly, the only two cancer cell lines resistant to KP372-1 toxicity in this study, MDA-MB-231 cells and H596 cells, were also NQO1 negative (Figures 6H and 6I), while the killing effects of KP372-1 on other cancer cell lines expressing NQO1 were effectively attenuated by dicoumarol (Figures 6H and 6I). β-lapachone showed a similar cytotoxicity profile as KP372-1 and was similarly antagonized by dicoumarol (Figure S6K).

It is known that a subset of NSCLC cell lines and tumors exhibit KEAP1 mutations which activate NRF2 (Dai et al., 2013; Singh et al., 2006). In these cells NRF2 then induces expression of NQO1, as well as a palette of antioxidant genes (Gorrini et al., 2013; Sporn and Liby, 2012; Thimmulappa et al., 2002). In KEAP wild-type cells, there is a good correlation between the cytotoxicity of KP372-1 and NQO1 expression (Figures S6L and S6M). In KEAP1 mutant cells, however, there is no clear correlation between the cytotoxicity of KP372-1 and the KEAP mutation (Figures S6L and S6M), suggesting the effects of overexpressed NQO1 may be counterbalanced by the enhanced antioxidant mechanism (Figures S6N and S6O).

The role of NQO1 in KP372-1 toxicity is further supported by in vivo data, which showed that the growth of the A549 xenografts was significantly suppressed by KP372-1 compared with vehicle (Figures 6J and 6K). In contrast, the growth of NQO1 knockout A549 xenografts was not suppressed by KP372-1 compared with vehicle (Figures 6L and 6M). Similarly, growth of NQO1 knockout H1299 xenografts was much less suppressed by KP372-1 (Figures 6N, 6O, and S6P) compared to wild-type H1299 xenografts (Figures 4D, 4E, and S4C).

KP372-1 is known to inhibit Akt kinase (Koul et al., 2006; Mandal et al., 2005, 2006; Zeng et al., 2006). Interestingly, our data showed that the effects of KP372-1 on the fluorescence of SoNar or roGFP1 were absent when A549 and H1299 cells were treated with different Akt inhibitors (Figures S6Q–S6T). Surprisingly and in contradistinction to previous reports that KP372-1 inhibited Akt phosphorylation in cancer cells (Koul et al., 2006; Mandal et al., 2005, 2006; Zeng et al., 2006), we found that KP372-1 treatment dramatically, transiently, and dose-dependently increased phosphorylation of Akt in A549 and H1299 cells (Figures 6G and S6U), which was not significantly affected by NQO1 inhibition or NQO1 knockout (Figure 6G). Such enhanced Akt phosphorylation induced by KP372-1 also occurred to varying extents in other cancer cell lines irrespective of their NQO1 expression level (Figure 6H). These data showed that KP372-1's action on NAD^+/NADH redox, oxidative stress, and viability of cancer cells was not due to the inhibition of this kinase.

NQO1 is a NAD(P)H-dependent oxidoreductase that catalyzes the 2-electron reduction of a broad range of quinones. β-lapachone was previously reported to exert its anti-tumor function by "bioactivation" by NQO1 to an unstable hydroquinone that rapidly undergoes a two-step oxidation back to the parent compound, perpetuating a futile redox cycle and generating superoxide in the process (Pink et al., 2000; Reinicke et al., 2005). We found that NAD(P)H was rapidly oxidized in the presence of both KP372-1 and trace amounts of NQO1 in vitro, monitored by either NAD(P)H endogenous fluorescence (Figures 6P and S6V) or SoNar (Figure S6W). The oxidation of NADH was accompanied by oxygen consumption (Figure 6Q) and generation of superoxide and hydrogen peroxide (Figures 6R and S6X). In these studies, greater than 1,000 molar equivalents of NADH were oxidized per molar equivalent of KP372-1 in 30 min (Figure 6P), suggesting that KP372-1 underwent NQO1-dependent redox cycling. In H1299 cells, oxygen consumption also significantly increased in the presence of KP372-1, which further increased with overexpression of NQO1 (Figure S6Y). Taken together, our findings provide evidence that NQO1-mediated futile redox cycling of KP372-1 (Figure 6S) induced oxidative stress and cell death in cancer cells.

Figure 6. NQO1 Catalyzes NAD(P)H-Dependent KP372-1 Redox Cycling and Promotes Cancer Cell Death

(A) Overexpression of NQO1, but not other NAD(P)H oxidases, increases KP372-1-induced NADH oxidation, H_2O_2 production, thiol oxidation, and cell death in H1299 cells.

(B) The NQO1 inhibitor dicoumarol, but not other pharmacologic inhibitors of ROS-generating enzymes, decreases KP372-1-induced NADH oxidation, H_2O_2 production, thiol oxidation, and cell death in A549 cells. For (A) and (B), after cells were treated with KP372-1, SoNar fluorescence was measured immediately, while Hyper and roGFP1 fluorescence were measured after 10 min.

(C–F) Knockout of NQO1 decreased KP372-1-induced cell death (C), NADH oxidation measured by SoNar fluorescence (D), H_2O_2 production measured by Hyper fluorescence (E), and thiol oxidation measured by roGFP1 fluorescence (F) in A549 cells.

(G) The effect of NQO1 inhibitor dicoumarol or NQO1 knockout on KP372-1-induced phosphorylation of Akt in A549 cells. Cells were treated with different concentrations of KP372-1 for 10 min.

(H) Phosphorylation of Akt in different cells treated with 0.5 μM KP372-1 at the indicated times.

(I) The effect of NQO1 inhibitor dicoumarol on KP372-1-induced cell death. Cells were exposed to a 4-hr pulse of KP372-1 either with or without 50 μM dicoumarol and then grown for 24 hr.

(J–O) The effects of KP372-1 on tumor growth of WT A549 (J and K), NQO1 knockout A549 (L and M), and NQO1 knockout H1299 (N and O) xenografts. Tumor-growth curves (J, L, and N) were measured in untreated or KP372-1-treated mice; error bars denote SEM (n = 8 in each group). Xenografts were dissected at day 38 (K and M) or day 28 (O), photographed (left), and weighted (right). Error bars indicate SEM.

(P) NQO1-catalyzed NADH oxidation in the presence of different concentrations of KP372-1. NADH was measured by its endogenous fluorescence. The concentrations of KP372-1 are indicated adjacent to each curve.

(Q) Oxygen consumption of NADH solution (600 μM) in the presence or absence of 1 μg/ml NQO1 and different concentrations of KP372-1. Oxygen levels were measured with a BD Oxygen Biosensor System.

(R) Superoxide production by a lucigenin chemiluminescence assay in an assay solution containing 600 μM NADH and KP372-1, in the presence or absence of 1 μg/ml NQO1 and/or 30 U/ml superoxide dismutase.

(S) Hypothetical model for KP372-1-mediated redox cycling. Error bars represent SEM. See also Figure S6.

DISCUSSION

The SoNar sensor described herein represents a substantial improvement for live cell NAD^+/NADH measurement over existing reporters. First, SoNar fluorescence is intrinsically ratiometric with two excitation wavelengths having opposing responses to NAD^+ and NADH, allowing quantitative determination of NAD^+ or NADH separately as well as ratiometrically. To our knowledge, such a dual-response property is unprecedented among genetically encoded sensors developed to date. In addition to its role in energy metabolism, NAD^+ also participates in a wide range of cellular processes, acting as precursor of signaling molecules such as cADPR and ADPR, and as a co-substrate of regulatory enzymes of significant importance, such as mono- or poly-ADP-ribose polymerases and Sirt family deacylases. Many of these enzymes are also important targets for drug discovery. SoNar is capable of reporting NAD^+ levels directly in vitro independent of NADH, and can be utilized in simple, continuous enzymatic assays, which may be amenable to high-throughput screening. Second, SoNar is an authentic reporter of the NAD^+/NADH ratio under physiological conditions. SoNar had an apparent K_d of ~5.0 μM for NAD^+, much lower than intracellular NAD^+ concentration, allowing the sensor to report the NAD^+/NADH ratio under physiological conditions accurately unaffected by the total NAD(H) pool. By contrast, the Frex sensor reports only NADH levels, while Peredox reports the cytosolic NADH level, partly compensated by the NAD^+ level, rather than the precise NAD^+/NADH ratio (Hung et al., 2011). Third, SoNar displays a superior rapid response and large dynamic range, and is very useful for the real-time tracking of subtle differences in cellular metabolic states. SoNar displays a 1,500% fluorescence change under different NAD^+/NADH ratios in vitro, almost 10-fold greater than that of Peredox and 2-fold greater than that of Frex, making it one of the most responsive genetic-encoded sensors currently available. SoNar responded well to conventional metabolic perturbations such as extraneous glucose, pyruvate, and lactate supplementation, or inhibition of energy metabolism pathways such as mitochondrial respiration, the mitochondrial NADH shuttle, glycolysis, and LDH. In live cell studies, the sensor displayed an 8-fold dynamic range, and was able to detect the response to added pyruvate as low as 5 μM, substantially outperforming either Frex or Peredox sensors. SoNar also performed nicely in in vivo imaging studies, exhibiting intense fluorescence and the ability to detect increases or decreases in NAD^+/NADH levels within normal physiological conditions. Our study showed that Peredox was not able to detect the decrease in the NAD^+/NADH ratio when cells were treated with lactate or an LDH inhibitor, as it was almost fully saturated by NADH in cells in the presence of 1 mM glucose (Hung et al., 2011). This deficiency complicates Peredox's usage for in vivo imaging, considering the normal range of blood glucose concentration.

Various studies suggested that the intracellular NAD^+/NADH pool is greatly reduced in many cancer cells compared to non-cancer cells, inferred by the lower lifetime of NADH endogenous fluorescence and increased mitochondrial free NADH, or lower ratio of the fluorescence intensity of FAD-to-NADH (Ostrander et al., 2010; Pradhan et al., 1995; Skala et al., 2007; Yu and Heikal, 2009); however, to our knowledge, the intracellular NAD^+/NADH ratio had not been rigorously quantified due to lack of appropriate quantitative non-invasive methodology. By monitoring SoNar's fluorescence, we provide direct evidence that the cytosolic NAD^+/NADH ratio is significantly reduced in certain cancer cell lines, such as H1299, U87, and MDA-MB-468. Further dissection of the metabolic pathways governing this ratio using enzyme inhibitors showed that these cancer cells were able to utilize low levels of glucose and exhibit high glycolytic activity, consistent with a previous report that H1299 cells overexpress pyruvate kinase M2 and display high rates of glycolysis (Christofk et al., 2008). For reference, we attach a diagram that explains the central role NAD^+/NADH plays in relevant metabolic pathways in this study (Figure S2K).

The intense fluorescence and large dynamic range of SoNar enabled its usage in robust high-throughput and real-time screening assays of small-molecule libraries that may affect cellular metabolism, which may be useful as probes for metabolic studies and as lead compounds for drug discovery. In contrast to many other high-throughput assays in drug discovery that target a single protein or enzyme, SoNar is multi-targeted as it is capable of reporting subtle perturbations in many pathways affecting energy metabolism, including glycolysis and mitochondrial respiration. Furthermore, the rapid response and high sensitivity greatly reduce the costs of and time needed for screening. Most of the compounds that we screened did not affect intracellular NAD^+ redox states; however, protein kinase inhibitor and phosphokinase inhibitor libraries had a significant percentage of hits, highlighting the regulatory roles of protein phosphorylation in cell metabolism. It is interesting that quite a few compounds among FDA-approved drugs and the NIH clinical collection also affect cellular metabolism. Further analysis may help to identify whether the effects of these drugs on metabolism are related to their anti-tumor mechanism and efficacy.

It is also interesting that only a small fraction of compounds that decrease the NAD^+/NADH ratio exhibited obvious cytotoxicity, whereas the majority of the compounds that increase the NAD^+/NADH ratio exhibited obvious cancer cell toxicity, among which β-lapachone, shikonin, and fascaplysin were potent, widely studied anti-tumor agents. Consistent with their effects on their NAD^+/NADH ratio as reported by the SoNar sensor, β-lapachone is known to be reduced by NQO1, which then enters into futile cycling, consumes NAD(P)H, and generates superoxide, while shikonin inhibits cancer cell glycolysis by targeting tumor pyruvate kinase M2 (Chen et al., 2011). The other compounds identified were not previously linked to cellular metabolism. The most potent compound that increases the NAD^+/NADH ratio and the most potent selective cancer-killing compound, KP372-1, was previously reported to exert inhibitory effects on PDK1/Akt signaling pathways, suppressing cell proliferation and inducing/sensitizing cells to apoptosis (Koul et al., 2006; Mandal et al., 2005, 2006; Zeng et al., 2006). Intriguingly, we found that the compound actually enhanced Akt phosphorylation, contradictory to previous reports, and that various specific Akt inhibitors had no significant impact on the NAD^+/NADH redox level. KP372-1 induced significant oxidative stress as shown by NAD(P)H depletion, H_2O_2 generation, and thiol oxidation. The PPP was activated to replenish NADPH for antioxidant enzyme catalysis. Further genetic and chemical screening showed that KP372-1 was reduced by NQO1 in the presence of

NAD(P)H, which enters into a futile redox cycle and generates superoxide; its anti-tumor activity was blocked by a specific NQO1 inhibitor or in isogenic NQO1 knockout cells. These data show that KP372-1's action on NAD^+/NADH redox, oxidative stress, and viability of cancer cells was due to NQO1-mediated futile redox cycling, and not the inhibition of Akt signaling. Kinase inhibitors have been very popular for dissecting signal transduction pathways and drug discovery. Although investigators are aware that inhibition of an off-target kinase may contribute to the observed biological effects of these inhibitors, the results reported here provide an interesting example that a distinct redox enzyme and mechanism are responsible for the selective cancer cell-killing effects of a well-known kinase inhibitor, rather than kinase inhibition itself. NQO1 was highly expressed in numerous cancer cells (Bey et al., 2007; Cullen et al., 2003; Pink et al., 2000). β-lapachone, an anti-tumor agent containing the quinone pharmacophore, can kill cancer cells overexpressing NQO1 regardless of cell cycle phase or p53 status. The quinone pharmacophore is particularly common in anti-tumor drugs, such as mitomycin C, β-lapachone, and 17-N-allylamino-17-demethoxygeldanamycin 17-AAG (Siegel et al., 2012). Unlike these compounds, KP372-1 does not contain a quinone pharmacophore. In view of the NQO1-catalyzed redox cycling of β-lapachone (Pink et al., 2000; Reinicke et al., 2005), we speculate the possible reaction mechanism of KP372-1, NAD(P)H, and NQO1 as follows (Figure 6S): KP372-1 contains a quinone mimic and can be reduced to the "hydro" form by NAD(P)H via a 2-electron reduction catalyzed by NQO1. The hydro form is presumably unstable and spontaneously auto-oxidizes to its original parent form, probably through an intermediate ($KP372\text{-}1(H)^{\cdot-}$), which consumes oxygen and generates superoxide. This redox cycling causes rapid and profound oxidation of NAD(P)H.

Most current NQO1 substrates developed for cancer therapy have problems in pharmacokinetics, tolerability, delivery, and bioavailability. For example, β-lapachone suffers from poor aqueous solubility and a short half-life in vivo (~20 min), which necessitates the use hydroxypropyl-β-cyclodextrin (HPβCD) as a solubility aid at the doses poorly tolerated (Bair, 2012; Blanco et al., 2010; Huang et al., 2012). We reasoned that KP372-1 could be a better candidate in future NQO1-dependent chemotherapies, as it is one magnitude more potent than β-lapachone; is capable of being administered orally; has a long half-life, large volume of distribution, and excellent bioavailability; and is very well tolerated by mice at the doses required to detect a significant anticancer effect. By in vivo imaging of tumor metabolism using the SoNar sensor, we also demonstrated that KP372-1 enters the tumor rapidly. Furthermore, identification of a non-quinone redox cycling agent like KP372-1 expands our scope and understanding of NQO1 and redox cycling agents. These compounds and their analogs can be further modified and investigated to develop better anti-tumor drugs.

In summary, we report that SoNar is a superior tool for tracking the intracellular NAD^+/NADH redox state and, therefore, subtle changes in cell metabolic status, as it is intensely fluorescent, is intrinsically ratiometric, and has a large dynamic range. These properties make it an ideal reagent for metabolic studies and drug discovery in cells or animals. Interestingly, we identified a potent NQO1-activated redox cycling and anti-tumor agent, KP372-1, which was previously used as (believed to be) an Akt inhibitor. Further studies on KP372-1 and its analogs might lead to therapeutic options for drug-resistant cancers. With the help of the SoNar sensor, we also identified many other compounds, including clinically used drugs that affect cellular metabolism. Although not investigated in this study owing to practical considerations of time, effort, and compound availability, it is possible that the clinical benefits of these drugs are less attributable to their reported targets or mechanism of action and, perhaps, more likely a consequence of effects on cellular metabolism.

EXPERIMENTAL PROCEDURES

Please see the Supplemental Experimental Procedures for additional details. All procedures involving animals were approved by the Institutional Animal Care and Use Committee of Shanghai.

Gene Construction and Protein Characterization

Gene construction and characterization of SoNar in vitro are described in Supplemental Experimental Procedures.

Live Cell Fluorescence Measurement Using Microplate Reader

Cells were harvested by trypsinization and counted by hemocytometer. Cells were washed and suspended in PBS (HyClone), and aliquots of cells were incubated at 37°C with different compounds during the measurement. Dual-excitation ratios were obtained by a Synergy 2 Multi-Mode Microplate Reader (BioTek). Detailed procedures can be found in the Supplemental Experimental Procedures.

Fluorescence Microscopy

For fluorescence microscopy, H1299-SoNar-, H1299-cpYFP-, H1299-Hyper-, and H1299-roGFP1-expressing cells were plated on a 35-mm glass-bottom dish with phenol red-free growth medium. Images were acquired using a high-performance fluorescent microscopy system equipped with Nikon Eclipse Ti-E automatic microscope, monochrome cooled digital camera head DS-Qi1 Mc-U2, and the highly stable Sutter Lambda XL light source. Raw data were exported to ImageJ software as 12-bit TIF for analysis. Detailed procedures can be found in the Supplemental Experimental Procedures.

Imaging NADH Metabolism in Living Animals

H1299-SoNar- and H1299-cpYFP-expressing cells (10×10^6) suspended in 0.1 ml serum-free RPMI1640 with an equal volume of BD Matrigel Matrix (BD Biosciences, 356237) were inoculated s.c. in the right axilla of each mouse. When tumor size reached 0.6–1.2 cm in diameter, mice were anesthetized intraperitoneally with sodium pentobarbital (100 mg/kg body weight), placed in a holding chamber, and given an intravenous tail vein injection with 100 mM sodium pyruvate (Invitrogen) or 600 μM KP372-1 (Echelon Biosciences) suspended in 0.9% NaCl in a total volume of 0.3 ml. The dual-excitation ratio imaging in tumor tissues expressing SoNar or cpYFP was obtained by a Kodak Multispectral FX imaging system (Carestream Molecular Imaging) with excitation filters 420 BP 20 nm and 490 BP 20 nm, and an emission filter 535 BP 50 nm (for both excitation wavelengths).

Chemical Screen and Analysis

All screened compounds were purchased from the National Compounds Resource Center (China) as stock solutions in DMSO. The majority of the compounds were arrayed in 96-well plates and diluted to 3 μM or 30 μM with PBS containing 25 mM glucose. We then transferred 25-μl chemical solutions from 96-well plates into black 384-well flat-bottom plates (Greiner Bio-One, Germany) using an eight-channel pipette and then immediately added 50 μl H1299-SoNar-expressing cell suspensions into each well using an eight-channel electronic pipette (50–1,250 μl), resulting in 1-μM and 10-μM final concentrations for most compounds. Each plate contained the following control wells: four to eight wells DMSO-only control, two to four wells controls with 1 mM pyruvate, and two to four wells controls with 5 mM oxamate. Fluorescence intensity was measured immediately by a Synergy 2 Multi-Mode Microplate

Reader (BioTek) with 420-nm or 485-nm excitation and 528-nm emission wavelengths. Analysis of screening data is described in Supplemental Experimental Procedures. The *I* value for every compound performed in our screen can be found in Table S2.

Metabolomics Analysis

The metabolomic analysis was performed by Metabolon (Durham). Detailed procedures can be found in the Supplemental Experimental Procedures.

Xenograft Studies

To test the anti-tumor activity of KP372-1 in vivo, nude mice (nu/nu, male 6- to 8-week-old, Shanghai SLAC Laboratory Animal Co.) were injected s.c. with 5×10^6 cells. Animals were divided randomly into control (vehicle), 10 mg/kg prevention, or 20 mg/kg prevention groups of eight each. Treatment was performed once daily by intragastric administration of KP372-1. Tumor formation was assessed every 2–3 days with calipers in all the groups. After 4–6 weeks, the tumors were dissected and weighed.

Statistical Analysis

Data are presented either as a representative example of a single experiment repeated at least in triplicate or as three or more experiments. Data obtained are represented as mean values ± SD or mean values ± SEM. All p values were obtained using unpaired two-tailed Student's t test. Values of $p < 0.05$ were considered statistically significant (*$p < 0.05$, **$p < 0.01$, and ***$p < 0.001$).

SUPPLEMENTAL INFORMATION

Supplemental Information includes six figures, four tables, and Supplemental Experimental Procedures and can be found with this article online at http://dx.doi.org/10.1016/j.cmet.2015.04.009.

AUTHOR CONTRIBUTIONS

Y.Y. and Q.H. designed the sensor, and Y.Y. and Y. Zhao designed the in vitro and in vivo imaging, metabolic screening, and target identification experiments. Y. Zhao, Q.H., N.S., A.W., and Y. Zou performed experiments. F.C., H.H., X.C., H.-M.Z., X.H., K.Y., Q.Z., X.W., J.Y., L.Z., X.Q., L.C., and Y.T. gave technical support and conceptual advice. Y.Y., Y. Zhao, and J.L. analyzed the data and wrote the manuscript.

ACKNOWLEDGMENTS

We thank Gary Yellen for the Peredox vector; Jim Remington for the roGFP vector; Jiahuai Han for the cDNA of Enox and Nox families; Hongbin Ji, Jianwen Liu, Jing Zheng, Ping Shi, Xuni Cao, Zhaoyang Ye, and Jia Yu for different cell lines; Guiping Li, Qiongyu Yan, Chunyuan Zhou, Qiuning Lin, Lei Xu, Rongkun Tao, Jianhua Wang, Zhengda Chen, and Wei Wang for technical assistance; and Stephanie Tribuna for secretarial assistance. This work was supported by the 973 Program (2013CB531200), NSFC (91313301, 31225008, 31071260, 31170815, 31470833, and 91013012), Specialized Research Fund for the Doctoral Program of Higher Education (20100074110010), Shanghai Science and Technology Commission (12JC1402900, 11DZ2260600, 15YF1402600), Dawn Program of the Shanghai Education Commission (11SG31), State Key Laboratory of Bioreactor Engineering, the 111 Project (B07023), and the Fundamental Research Funds for the Central Universities, as well as NIH grants (to J.L.) HL061795, HL048743, and HL108630.

Received: October 23, 2014
Revised: February 26, 2015
Accepted: April 3, 2015
Published: May 5, 2015

REFERENCES

Bair, J. (2012). The development of deoxynyboquinone as a personalized anticancer compound. Dissertation (University of Illinois at Urbana–Champaign).

Belousov, V.V., Fradkov, A.F., Lukyanov, K.A., Staroverov, D.B., Shakhbazov, K.S., Terskikh, A.V., and Lukyanov, S. (2006). Genetically encoded fluorescent indicator for intracellular hydrogen peroxide. Nat. Methods *3*, 281–286.

Bey, E.A., Bentle, M.S., Reinicke, K.E., Dong, Y., Yang, C.R., Girard, L., Minna, J.D., Bornmann, W.G., Gao, J., and Boothman, D.A. (2007). An NQO1- and PARP-1-mediated cell death pathway induced in non-small-cell lung cancer cells by beta-lapachone. Proc. Natl. Acad. Sci. USA *104*, 11832–11837.

Blanco, E., Bey, E.A., Khemtong, C., Yang, S.G., Setti-Guthi, J., Chen, H., Kessinger, C.W., Carnevale, K.A., Bornmann, W.G., Boothman, D.A., and Gao, J. (2010). Beta-lapachone micellar nanotherapeutics for non-small cell lung cancer therapy. Cancer Res. *70*, 3896–3904.

Cairns, R.A., Harris, I.S., and Mak, T.W. (2011). Regulation of cancer cell metabolism. Nat. Rev. Cancer *11*, 85–95.

Chen, J., Xie, J., Jiang, Z., Wang, B., Wang, Y., and Hu, X. (2011). Shikonin and its analogs inhibit cancer cell glycolysis by targeting tumor pyruvate kinase-M2. Oncogene *30*, 4297–4306.

Christofk, H.R., Vander Heiden, M.G., Harris, M.H., Ramanathan, A., Gerszten, R.E., Wei, R., Fleming, M.D., Schreiber, S.L., and Cantley, L.C. (2008). The M2 splice isoform of pyruvate kinase is important for cancer metabolism and tumour growth. Nature *452*, 230–233.

Cong, L., Ran, F.A., Cox, D., Lin, S., Barretto, R., Habib, N., Hsu, P.D., Wu, X., Jiang, W., Marraffini, L.A., and Zhang, F. (2013). Multiplex genome engineering using CRISPR/Cas systems. Science *339*, 819–823.

Cullen, J.J., Hinkhouse, M.M., Grady, M., Gaut, A.W., Liu, J., Zhang, Y.P., Weydert, C.J., Domann, F.E., and Oberley, L.W. (2003). Dicumarol inhibition of NADPH:quinone oxidoreductase induces growth inhibition of pancreatic cancer via a superoxide-mediated mechanism. Cancer Res. *63*, 5513–5520.

Dai, B., Yoo, S.Y., Bartholomeusz, G., Graham, R.A., Majidi, M., Yan, S., Meng, J., Ji, L., Coombes, K., Minna, J.D., et al. (2013). KEAP1-dependent synthetic lethality induced by AKT and TXNRD1 inhibitors in lung cancer. Cancer Res. *73*, 5532–5543.

Dooley, C.T., Dore, T.M., Hanson, G.T., Jackson, W.C., Remington, S.J., and Tsien, R.Y. (2004). Imaging dynamic redox changes in mammalian cells with green fluorescent protein indicators. J. Biol. Chem. *279*, 22284–22293.

Gorrini, C., Harris, I.S., and Mak, T.W. (2013). Modulation of oxidative stress as an anticancer strategy. Nat. Rev. Drug Discov. *12*, 931–947.

Huang, X., Dong, Y., Bey, E.A., Kilgore, J.A., Bair, J.S., Li, L.S., Patel, M., Parkinson, E.I., Wang, Y., Williams, N.S., et al. (2012). An NQO1 substrate with potent antitumor activity that selectively kills by PARP1-induced programmed necrosis. Cancer Res. *72*, 3038–3047.

Hung, Y.P., Albeck, J.G., Tantama, M., and Yellen, G. (2011). Imaging cytosolic NADH-NAD(+) redox state with a genetically encoded fluorescent biosensor. Cell Metab. *14*, 545–554.

Koul, D., Shen, R., Bergh, S., Sheng, X., Shishodia, S., Lafortune, T.A., Lu, Y., de Groot, J.F., Mills, G.B., and Yung, W.K. (2006). Inhibition of Akt survival pathway by a small-molecule inhibitor in human glioblastoma. Mol. Cancer Ther. *5*, 637–644.

Le, A., Cooper, C.R., Gouw, A.M., Dinavahi, R., Maitra, A., Deck, L.M., Royer, R.E., Vander Jagt, D.L., Semenza, G.L., and Dang, C.V. (2010). Inhibition of lactate dehydrogenase A induces oxidative stress and inhibits tumor progression. Proc. Natl. Acad. Sci. USA *107*, 2037–2042.

Mandal, M., Kim, S., Younes, M.N., Jasser, S.A., El-Naggar, A.K., Mills, G.B., and Myers, J.N. (2005). The Akt inhibitor KP372-1 suppresses Akt activity and cell proliferation and induces apoptosis in thyroid cancer cells. Br. J. Cancer *92*, 1899–1905.

Mandal, M., Younes, M., Swan, E.A., Jasser, S.A., Doan, D., Yigitbasi, O., McMurphey, A., Ludwick, J., El-Naggar, A.K., Bucana, C., et al. (2006). The Akt inhibitor KP372-1 inhibits proliferation and induces apoptosis and anoikis in squamous cell carcinoma of the head and neck. Oral Oncol. *42*, 430–439.

Ostrander, J.H., McMahon, C.M., Lem, S., Millon, S.R., Brown, J.Q., Seewaldt, V.L., and Ramanujam, N. (2010). Optical redox ratio differentiates breast cancer cell lines based on estrogen receptor status. Cancer Res. *70*, 4759–4766.

Pink, J.J., Planchon, S.M., Tagliarino, C., Varnes, M.E., Siegel, D., and Boothman, D.A. (2000). NAD(P)H:Quinone oxidoreductase activity is the

principal determinant of beta-lapachone cytotoxicity. J. Biol. Chem. *275*, 5416–5424.

Pradhan, A., Pal, P., Durocher, G., Villeneuve, L., Balassy, A., Babai, F., Gaboury, L., and Blanchard, L. (1995). Steady state and time-resolved fluorescence properties of metastatic and non-metastatic malignant cells from different species. J. Photochem. Photobiol. B *31*, 101–112.

Ran, F.A., Hsu, P.D., Wright, J., Agarwala, V., Scott, D.A., and Zhang, F. (2013). Genome engineering using the CRISPR-Cas9 system. Nat. Protoc. *8*, 2281–2308.

Reinicke, K.E., Bey, E.A., Bentle, M.S., Pink, J.J., Ingalls, S.T., Hoppel, C.L., Misico, R.I., Arzac, G.M., Burton, G., Bornmann, W.G., et al. (2005). Development of beta-lapachone prodrugs for therapy against human cancer cells with elevated NAD(P)H:quinone oxidoreductase 1 levels. Clin. Cancer Res. *11*, 3055–3064.

Siegel, D., Yan, C., and Ross, D. (2012). NAD(P)H:quinone oxidoreductase 1 (NQO1) in the sensitivity and resistance to antitumor quinones. Biochem. Pharmacol. *83*, 1033–1040.

Singh, A., Misra, V., Thimmulappa, R.K., Lee, H., Ames, S., Hoque, M.O., Herman, J.G., Baylin, S.B., Sidransky, D., Gabrielson, E., et al. (2006). Dysfunctional KEAP1-NRF2 interaction in non-small-cell lung cancer. PLoS Med. *3*, e420.

Skala, M.C., Riching, K.M., Gendron-Fitzpatrick, A., Eickhoff, J., Eliceiri, K.W., White, J.G., and Ramanujam, N. (2007). In vivo multiphoton microscopy of NADH and FAD redox states, fluorescence lifetimes, and cellular morphology in precancerous epithelia. Proc. Natl. Acad. Sci. USA *104*, 19494–19499.

Sporn, M.B., and Liby, K.T. (2012). NRF2 and cancer: the good, the bad and the importance of context. Nat. Rev. Cancer *12*, 564–571.

Thimmulappa, R.K., Mai, K.H., Srisuma, S., Kensler, T.W., Yamamoto, M., and Biswal, S. (2002). Identification of Nrf2-regulated genes induced by the chemopreventive agent sulforaphane by oligonucleotide microarray. Cancer Res. *62*, 5196–5203.

Vander Heiden, M.G. (2011). Targeting cancer metabolism: a therapeutic window opens. Nat. Rev. Drug Discov. *10*, 671–684.

Vander Heiden, M.G., Cantley, L.C., and Thompson, C.B. (2009). Understanding the Warburg effect: the metabolic requirements of cell proliferation. Science *324*, 1029–1033.

Warburg, O. (1956). On the origin of cancer cells. Science *123*, 309–314.

Williamson, D.H., Lund, P., and Krebs, H.A. (1967). The redox state of free nicotinamide-adenine dinucleotide in the cytoplasm and mitochondria of rat liver. Biochem. J. *103*, 514–527.

Yamada, K., Hara, N., Shibata, T., Osago, H., and Tsuchiya, M. (2006). The simultaneous measurement of nicotinamide adenine dinucleotide and related compounds by liquid chromatography/electrospray ionization tandem mass spectrometry. Anal. Biochem. *352*, 282–285.

Yang, H., Yang, T., Baur, J.A., Perez, E., Matsui, T., Carmona, J.J., Lamming, D.W., Souza-Pinto, N.C., Bohr, V.A., Rosenzweig, A., et al. (2007). Nutrient-sensitive mitochondrial NAD+ levels dictate cell survival. Cell *130*, 1095–1107.

Yu, Q., and Heikal, A.A. (2009). Two-photon autofluorescence dynamics imaging reveals sensitivity of intracellular NADH concentration and conformation to cell physiology at the single-cell level. J. Photochem. Photobiol. B *95*, 46–57.

Zeng, Z., Samudio, I.J., Zhang, W., Estrov, Z., Pelicano, H., Harris, D., Frolova, O., Hail, N., Jr., Chen, W., Kornblau, S.M., et al. (2006). Simultaneous inhibition of PDK1/AKT and Fms-like tyrosine kinase 3 signaling by a small-molecule KP372-1 induces mitochondrial dysfunction and apoptosis in acute myelogenous leukemia. Cancer Res. *66*, 3737–3746.

Zhao, Y., and Yang, Y. (2015). Profiling metabolic states with genetically encoded fluorescent biosensors for NADH. Curr. Opin. Biotechnol. *31*, 86–92.

Zhao, Y., Jin, J., Hu, Q., Zhou, H.M., Yi, J., Yu, Z., Xu, L., Wang, X., Yang, Y., and Loscalzo, J. (2011). Genetically encoded fluorescent sensors for intracellular NADH detection. Cell Metab. *14*, 555–566.